Advanced Powder Technology 37 (2026) 105148

Contents lists available at ScienceDirect

Advanced Powder Technology

journal homepage: www.elsevier.com/locate/apt

Original Research Paper

Maltodextrin spray drying in a compact radial multizone dryer – First pilot plant findings

Santanu Dey, Thomas Tourneur, Axel de Broqueville, Armand Béché, Juray De Wilde *

Université catholique de Louvain, Institute of Mechanics, Materials and Civil Engineering (IMMC), Materials and Process Engineering (IMAP), Place Sainte Barbe 2, 1348 Louvain-la-Neuve, Belgium

ARTICLE INFO

Article history:
Received 5 October 2025
Received in revised form 24 November 2025
Accepted 3 December 2025
Available online 11 December 2025

ABSTRACT

A novel compact radial multizone dryer (RMD) has been tested at the pilot scale. In the radial centre of the chamber, hot air and the atomized solution are injected axially and counter current. In the periphery, mild temperature air is injected through multiple short vortex chambers to generate a rotational motion in the chamber and ensure high-G intensified drying and separation of the produced powder and hot drying air. The RMD allows fast initial drying of the injected droplets with hot air in the radial centre and fast evacuation of the initially dried powder to the periphery for final drying with mild temperature air. First, dry and water evaporation tests were carried out to gain insight in the flow pattern and temperature profile in the chamber. Next, a 4.5 min duration spray drying test was carried out using a 40 % maltodextrin model solution at a solution feed rate of 16.1 g/s. The tests demonstrated the working principle and performance of the RMD. Powder recovery and quality, as well as energy efficiency are discussed.

1. Introduction

Spray drying is used to convert a dispersed solution or suspension into a dry, fine powder. Air or inert gas is used to evaporate the solvent. Heat sensitive materials require mild temperature operation. Conventional spray dryers are large because of the required droplet/particle-air contact time. The efficiency of interfacial mass and heat transfer is limited by the low maximum slip velocity between the droplets/particles and drying air – the so-called terminal velocity determined by earth gravity [1]. This also limits the air velocity that can be applied, as entrainment of particles with the air needs to be avoided. Furthermore, supplying the required energy with mild-temperature air requires high air flow rates. Combined with low air velocities, this results in large spray dryer cross sectional surface areas.

Interfacial mass and heat transfer can be intensified by operation at higher slip velocity and using high temperature air. Proper contact with the latter is essential to prevent degradation of the product. The Radial Multizone Dryer (RMD) design (Fig. 1) is partially based on the use of a vortex chamber to generate a high-G rotating fluidized bed in static geometry (RFB-SG) [2]. High-G operation allows operation at higher slip velocities and related intensification of interfacial mass, heat and momentum transfer. For given gas flow rate, the strength of the centrifugal force is determined by the tangential air inlet velocity, i.e. the number of slots of the vortex chamber and their size, to be adjusted for the density and diameter of the particles to be retained in the chamber [3,4]. In the RMD, vortex chambers are used to generate a centrifugal field and achieve fast evacuation of produced particles to the periphery where drying is completed with mild temperature air. To achieve fast initial drying and improve the energy efficiency, hot air and the atomized solution or suspension are injected counter current in the axial direction in the radial centre of the RMD. Multiple short vortex chambers installed at different heights in the chamber are used to reduce air consumption and control the axial motion in the periphery of the chamber. Whereas the drying air is evacuated via a central air exhaust, separate solids outlets are foreseen in the periphery of the chamber. The RMD applies radial multi-zone operation, in contrast to the previously tested axial multi-zone operation [26].

The hydrodynamics of rotating fluidized beds in a single vortex chamber has been extensively studied [5–9], as well as various drying applications [10–14]. Scale-up issues were discussed by Li et al. [27]. Comparison with conventional fluidized bed drying showed that ca. one order magnitude process intensification can be achieved by high-G operation [15–18]. It was also shown that the gas flow rate can be varied in a wide range with limited effect on the bed density or solids losses with the exhaust gas [11,18].

* Corresponding author.
E-mail address: juray.dewilde@uclouvain.be (J. De Wilde).

https://doi.org/10.1016/j.apt.2025.105148
0921-8831/

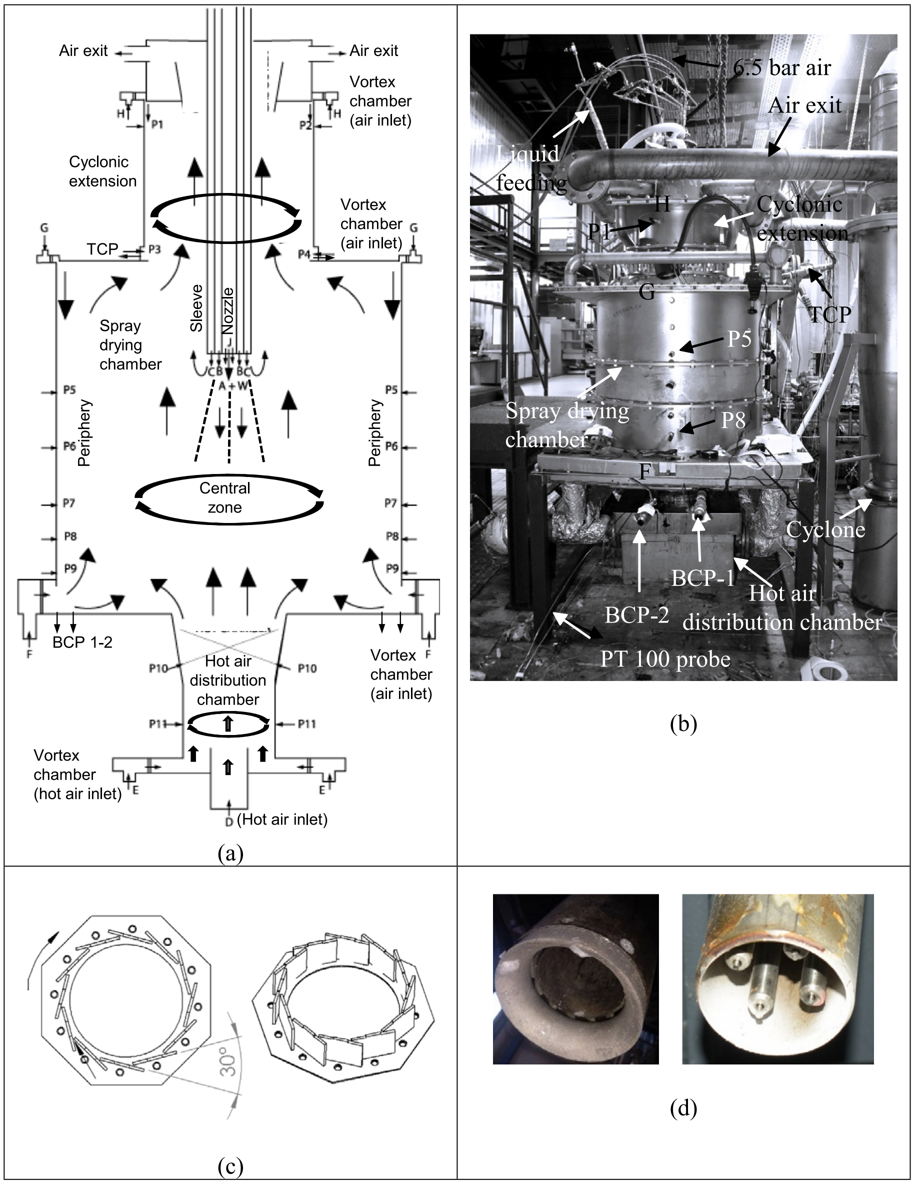

Fig. 1. (a) Schematic drawing with labelled air streams and (b) Picture of the pilot plant Radial Multizone Dryer. (c) Example vortex chamber; (d) Top end protective sleeve and 4 atomization nozzles in the central tube of the protective sleeve.

This flexibility and high-G intensified momentum transfer allowed Eliaers et al. [26] to coat a cohesive powder and control agglomeration using vortex chamber technology. Because of the very short gas–solid contact times that can be achieved, the use of vortex chambers for carrying out fast chemical reactions, combustions [19] or for managing the heat of reaction [20 21 3 22 23] was considered. Finally, high-G intensified gas-solids contact and gas-solids separation can eventually be combined with high-G intensified particle segregation [24,25].

The current paper reports tests on a large pilot plant RMD, designed following successful tests with a small pilot plant RMD. Design modifications were made to improve the hot air utilization and fine particle recovery. They are discussed hereafter, along with the experimental set-up and procedures. The paper then first shows detailed temperature measurements during a dry run and when evaporating water. These measurements allow to confirm the operating principle of the RMD and to gain some insight in the complex flow pattern. Next, the RMD performance during a spray drying test is discussed, in terms of powder recovery and quality and in terms of energy efficiency.

2. Experimental set up

The RMD was designed based on experience with smaller-scale lab and pilot RMD's [11,15,16,26 28 29]. Figs. 1a and b show a schematic drawing and a picture of the RMD. A schematic drawing of a vortex chamber and pictures of the protective sleeve containing the two-fluid spray nozzles are shown in Figs. 1c and d. The RMD consists of four main parts: a wide cylindrical spray drying chamber with a vortex chamber against its top and bottom end walls, a hot air distribution chamber, a cyclonic extension with an additional vortex chamber, and a cylindrical protective sleeve penetrating the spray drying chamber in which the spray nozzles are mounted. To ensure all droplets / particles are sufficiently fast entrained by the counter current injected hot air, the latter is introduced at high velocity through a 270 mm diameter opening. Optimal contact between the hot air and the droplets, however, requires radial expansion of the hot air inside the spray drying chamber and avoiding symmetry breaking. Therefore, a radial dual hot air distribution design was applied (D and E streams), making use of an air splitter. The outer air is fed rotating (E stream, Fig. 1a), making use of 12 tangential injection slots, and a conical outlet end is foreseen. The hot air that is fed centrally is non-rotating to prevent generation of a low pressure zone in the centre that could cause internal recirculation and attract injected droplets. As for the spray drying chamber, because of the fast drying, formation of a thick rotating fluidized bed in the RMD is not expected. Dilute operation results in high centrifugal forces and important secondary flows resulting from the presence of the end walls [2,5]. Furthermore, even when the slots of a vortex chamber extend over its entire length, the gas enters the chamber non-uniformly and preferentially in the near-end wall regions, where it faces a lower centrifugal pressure. For this reason and to minimize air consumption, two short vortex chambers were introduced when scaling up the RMD, one placed in the vicinity of each end wall. The bottom vortex chamber (F stream) has 16 slots, 1.625 cm^2 per slot, the top vortex chamber (G stream) has 24 slots, 0.2917 cm^2 per slot. This also allows to generate a centrifugal pressure difference between the two vortex chambers, which can be used to control the axial motion in the periphery. The length-to-diameter ratio (L/D) is an important design parameter. Decreasing L/D was observed to improve the flow stability, but sufficient distance between the spray nozzles and the hot air inlet needs to be foreseen. Dry particles are collected via bottom and top collection ports (BCP / TCP) in the end walls of the spray drying chamber. The K air stream serves to cool the bottom end plate of the spray drying chamber through which the hot air enters and to cool the particles evacuated via the bottom collection ports. The solution is atomized using 4 two-fluid spray nozzles (Fig. 1d) [30], allowing independently setting the mean droplet size and liquid injection flow rate. Nozzles were operated in parallel to ensure a high droplet density in the radial centre of the chamber and the nozzle type was selected to provide a certain liquid injection velocity. The protective sleeve (Fig. 1d) for the nozzles has a complex design allowing secondary air injection (B, C and J streams), apart from the atomization air (A stream) to keep the nozzles and sleeve clean. To achieve the latter, the C stream is rotating. The cyclonic chamber serves reducing the loss of fines with the exhaust air. To increase the centrifugal force, it is equipped with an additional vortex chamber with 16 slots, 0.375 cm^2 per slot, through which the H stream is fed. An extra solids outlet evacuates the captured fines.

Fig. 2 shows the flow sheet of the pilot plant. Air is fed using a 68.9 kW Robuschi compressor (833 mbar) and a 9.74 kW Aerzen blower (236 mbar). The C, H, J, K, and G streams (Figs. 1a & 2) were electrically heated to 70 °C, the B, D, E and F streams to respectively 286 °C, 331 °C, 295 °C and 102 °C. Pumps feed water or liquid solution from storage tanks mounted on balances for flow rate measurement. The pumps are provided with internal recycle and ball valves are used to set the target water and solution flow rates to the RMD. Atomization air at 6.5 bar is fed using a Boge C25 compressor (A stream). Table 1 shows the various air flow rates, whereas Table 2 shows the air injection velocities for the four vortex chambers, assuming uniform air distribution.

Table 1
Various air feed flow rates into the RMD unit. Unit: m^3/hr.

B	D	E	F	C	H	J	K	G
111	716	1132	175	68	97	49	29	126

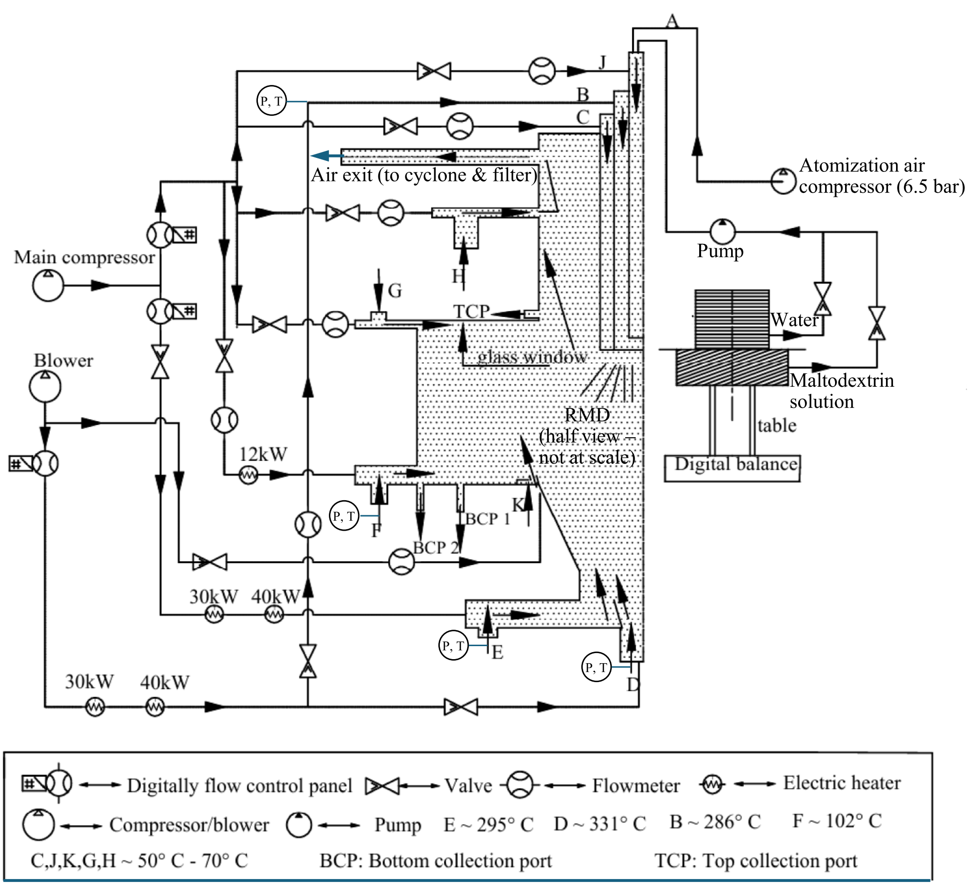

Fig. 2. Schematic diagram of the complete spray drying unit with the RMD (half shown), air blower and compressors, air heaters, liquid feed vessel and pump. BCP: bottom collection port, TCP: top collection port for the produced powder.

Table 2
Air injection velocity through the slots of the different vortex chambers in the RMD unit.

Inlet slot	E	F	G	H
Injection Velocity (m/s)	19	19	50	45
Number of slots	12	16	24	16
Area of slots (cm^2)	13.5	1.625	0.2917	0.375

Figs. 3a and b show various dimensions of the RMD and the location of the various measurement and sample ports. The total height of the set-up is 2.3 m, the diameter of the spray drying chamber 800 mm. Looking downward, the rotational motion in the RMD is in the clockwise direction. Pt 100 temperature sensors are used along with a Gefran TK pressure transmitter. The various measurement ports that can be used for sensor or probe insertion at different radial positions are shown in Fig. 1a and Fig. 3. After insertion, a sensor is kept at a particular location for 2–3 min until a stable reading is observed and then another 30 s for averaging purposes. Ports P1-P4 are located in the cyclonic extension, with P1 and P2 diametrically opposed at one elevation. Ports P3 and P4 are located somewhat lower and are not perfectly diametrically opposed. P4 is also located 7 mm below P3. Ports P5-P9 are located in the main spray drying chamber. Ports P5 are the highest up and located below the spray nozzles, and 285 mm below the bottom of the cyclonic extension. Ports P9 are found just above the bottom vortex chamber in the spray drying chamber. P5-P9 are quadrupled, every 90° in the rotational direction (Fig. 3b) and identified as Pi(0°), (90°), (180°) and (270°). The hot air distribution chamber has four ports. P10(l) (left) and P10(r) (right) are at same height, but with the sensor introduced under a 20° angle. As a result, when a sensor is introduced with half of its length, the sensor tip is at mid height in the hot chamber. With a sensor introduced at full length, the sensor tip is close to the top of the hot chamber. P11 (l) and P11(r) at same height, just above the bottom most vortex chamber (E stream). Another two thermocouples measure the air exit temperature. A National Instrument data acquisition system controlled by LabVIEW is used to save data with a sampling rate of 1 Hz.

Prior to the spray drying test, dry run and water evaporation tests serve gaining insight in the flow, temperature and evaporation patterns and identifying acceptable spray drying conditions. Comparison of the temperature profiles in a dry test and during water evaporation allows identifying where evaporation takes place, verifying droplets do not penetrate the hot air distribution chamber, and ensuring that the temperature in the periphery is sufficiently low. Complete evaporation and eventual asymmetric distribution of the atomized liquid in the chamber are visually verified.

Spray drying requires a specific start-up procedure. After setting the air flow rates and feed temperatures, the RMD unit is heated until a steady air exit temperature of 209 ± 1 °C is reached. Next, water is evaporated at 10.4 g/s until a new steady air exit temperature is observed. Critical temperatures are verified at this stage. To start spray drying, the liquid feed to the spray nozzles is switched from water to an aqueous 40 % maltodextrin solution and the liquid flow rate increased to 16.1 g/s to operate at constant water evaporation capacity of ca. 10 g/s. This minimized changes in the temperature profile in the RMD. The spray drying time was limited to 4.5 min. This brings the total weight of solution sprayed to 4.34 kg, the total weight maltodextrin spray dried to 1.738 kg. The shut-down procedure is also important as it can affect the quality of the powder recovered from inside the RMD and even in the solids recovery vessels. To avoid overheating the produced powder, the air heaters are shut down first, then the liquid flow is reduced gradually while progressively increasing the cold air flow rates and reducing the hot air flow rates.

3. Dry run

The dry test was done with the above-mentioned conditions except the A stream and with the air exit temperature at 202–206 °C. Fig. 4a shows the radial temperature profiles in the cyclonic extension measured through P1-P4 (Fig. 3a). In the immediate

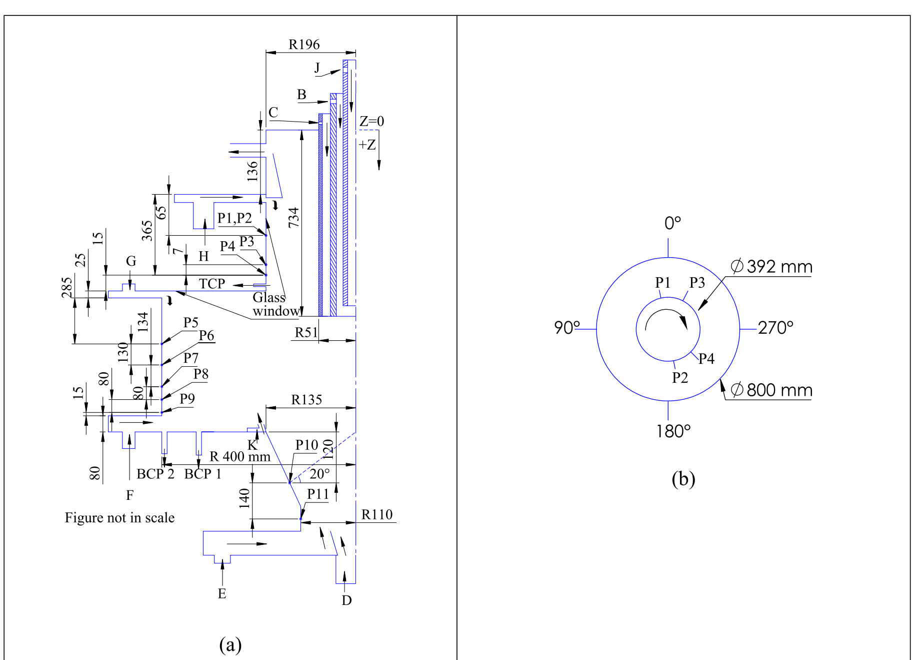

Fig. 3. (a) Side view (half shown) and (b) Top view of the positions of the different temperature measurement ports in the RMD unit and its most important dimensions.

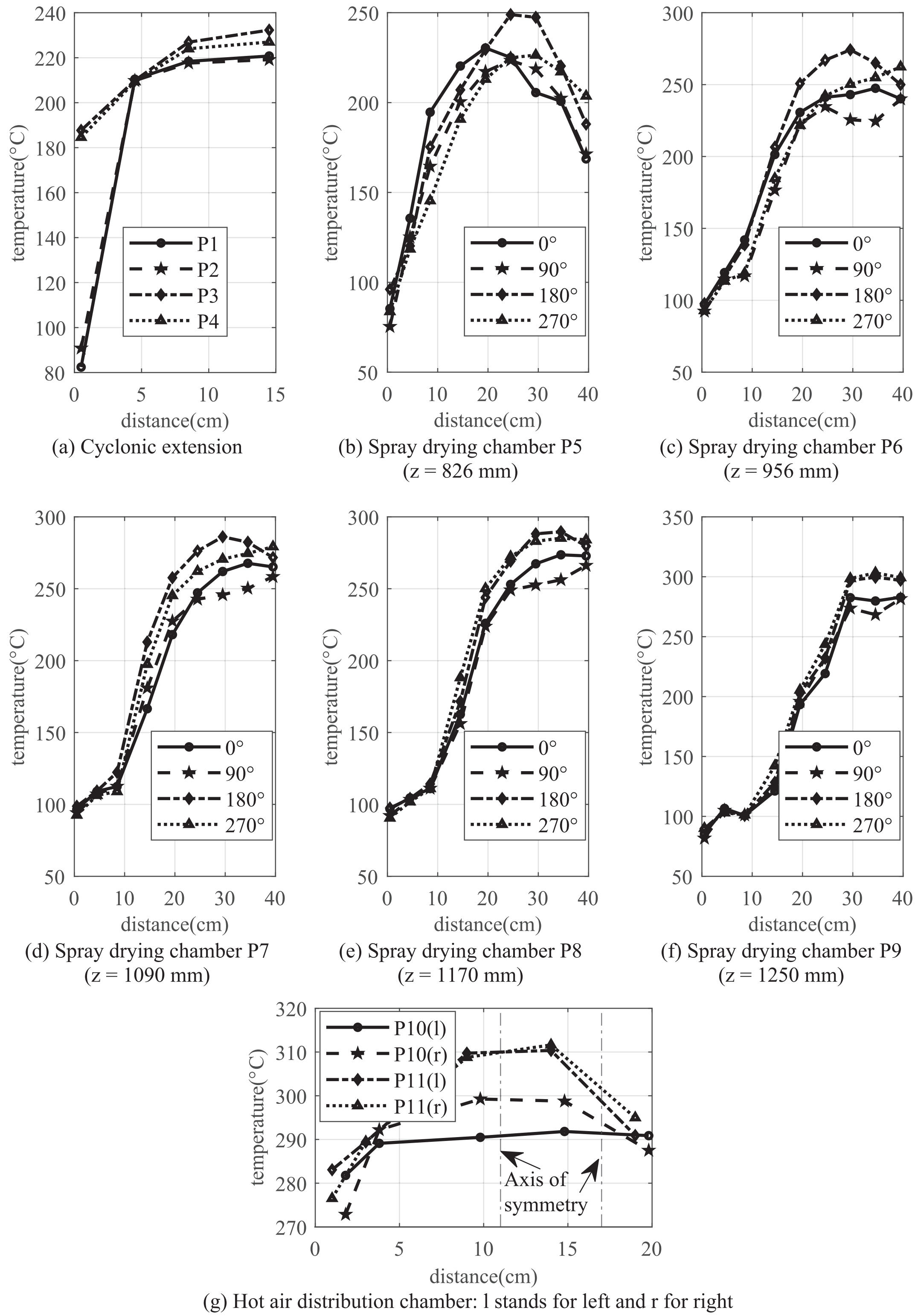

Fig. 4. Temperature profiles in the cyclonic extension, spray drying chamber and hot air distribution chamber during dry run. For all figures, the axis of symmetry is at maximum distance except for Figs. 4a and 4g in which the axis of symmetry is indicated by a dotted line. Distance from probe insertion point. Location of z = 0 – see Fig. 3a.

vicinity of the cylindrical wall (distance = 0), P1 and P2 are at ca. 80–90 °C, significantly lower than P3 and P4. This is explained by the downflow of the air injected in the top vortex chamber at 70 °C (H stream). The near-wall temperature of ca. 185 °C in P3 and P4 indicates this near-wall downflow of mild-temperature air does not reach the bottom of the cyclonic extension, so that the observed temperatures are mainly determined by the temperature of the air exiting the spray drying chamber. The latter is also the case in all points more away from the cylindrical wall, making temperatures also more uniform. The temperatures in P1 and P2 are still ca. 10 °C lower as a result of mixing with the 70 °C H stream. Comparison of the P1 and P2 temperature profiles shows good radial symmetry in the cyclonic extension. Some heat losses through the non-insulated wall should be taken into account.

Figs. 4b–f show the radial temperature profiles measured in the spray drying chamber through P5(0°, 90°, 180°, 270°)-P9(0°, 90°, 180°, 270°). The hot air is radially dispersed from bottom (P9) to top (P5), but the mild temperature air injected through the vortex chambers and the hot air remain well segregated, confirming the working principle of the RMD. With the hot air (D and E stream) fed at 295–331 °C, the lower temperatures near the radial centre of the chamber show penetration of mild temperature air coming from the atomizers and sleeve. Below the sleeve (P5), the maximum temperature has decreased to 225–250 °C, the temperature

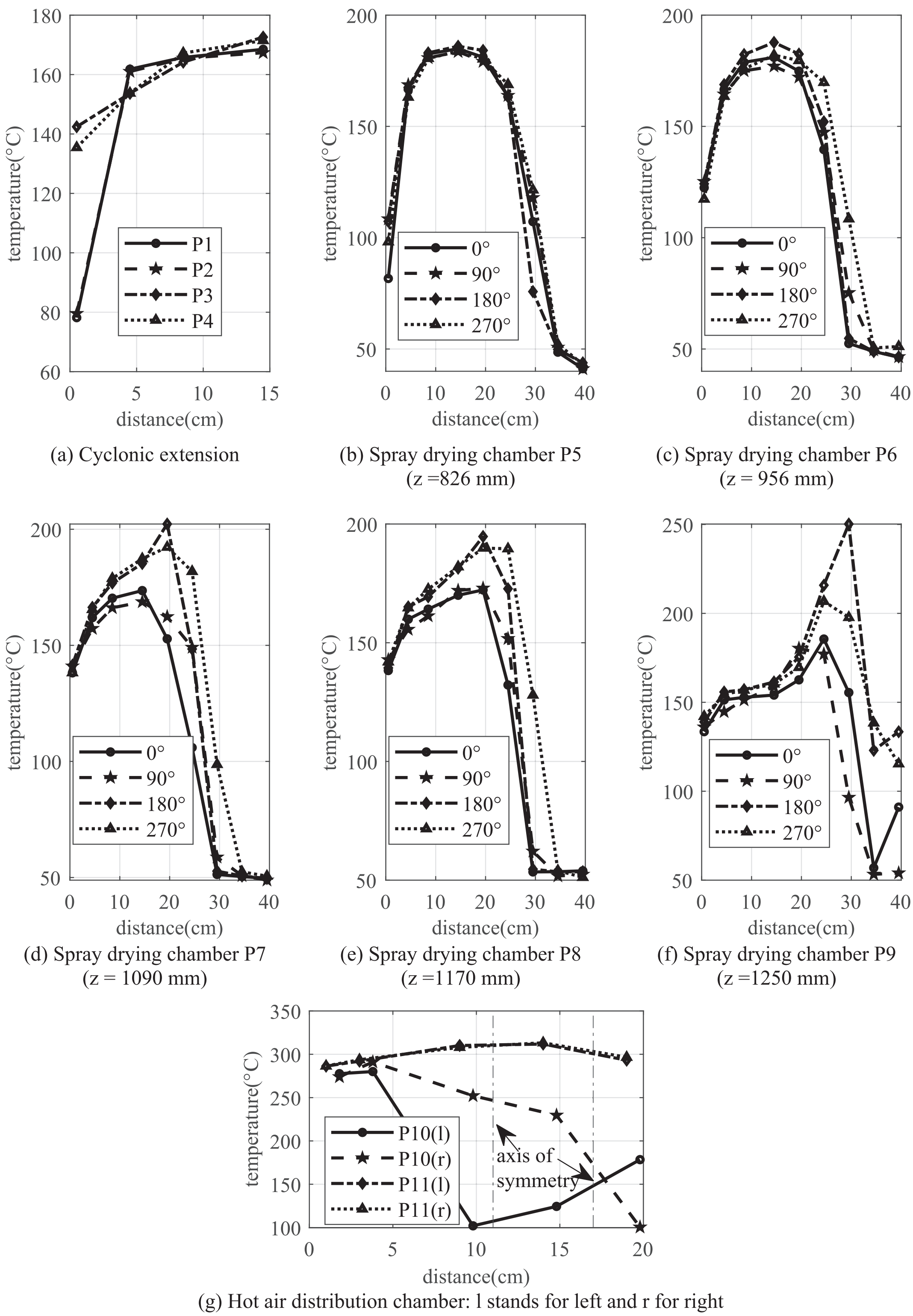

(a) Cyclonic extension

(b) Spray drying chamber P5 (z =826 mm)

(c) Spray drying chamber P6 (z = 956 mm)

(d) Spray drying chamber P7 (z = 1090 mm)

(e) Spray drying chamber P8 (z =1170 mm)

(f) Spray drying chamber P9 (z =1250 mm)

(g) Hot air distribution chamber: l stands for left and r for right

Fig. 5. Temperature profiles in the cyclonic extension, spray drying chamber and hot air distribution chamber during water evaporation. For all figures, the axis of symmetry is at maximum distance except for Figs. 4a and 4g in which the axis of symmetry is indicated by a dotted line. Distance from probe insertion point. Location of z = 0 – see Fig. 3a.

in the radial centre to 170–205 °C. Comparison of the temperature profiles measured through ports P5(0°), P5(90°), P5(180°) and P5 (270°) shows slight tangential asymmetry. The atomization air penetrates the hot air in the radial centre and bypassing of the two air streams does not occur. Minor atomization air deflection towards one side is also seen in the P6, P7 and P8 temperature profiles. At P7 and P8 elevation, the max temperature has increased to 250–290 °C, at P9 to 270–300 °C. Mild temperature atomisation air penetrates as low as P9, with the temperatures in the radial centre 260–285 °C at P7 and P8 elevation and 265–300 °C at P9.

The temperatures in the vicinity of the cylindrical wall of the spray drying chamber are all below 100 °C. Despite some asymmetry, the near-wall temperatures at P5 elevation are clearly affected by the G stream injected through the top vortex chamber at 70 °C, indicating a descending air stream in the periphery over at least than 25 cm or more than 1/3 of the main chamber length. The near-wall temperatures at P6-P8 elevations are, on the other hand, clearly determined by the F stream fed through the bottom vortex chamber at 102 °C, suggesting up flow in that region. The lower near-wall temperatures of ca. 85 °C observed in P9 show, however, the existence of a thin layer of 70 °C air descending all the way down, against the cylindrical wall, as a result of the centrifugal pressure difference between top and bottom. This layer is initially compressed by the high centrifugal pressure in the top of the chamber and then progressively expands towards the P9 elevation where it is captured by the temperature measurements. Radially inward flow is also expected to take place in the bottom section of the chamber where the centrifugal pressure is lower, but radial mixing of hot and mild temperature air is seen to be limited. The latter is explained by the axially upward parallel flow of hot air and mild temperature air – hot air in the radial centre and mild temperature air in the periphery but slightly away from the cylindrical wall.

The temperature measurements in the hot air distribution chamber (Fig. 4g) reveal some heat losses between the air heaters and the hot air inlet, with ca. 20 °C lower than expected D (330 °C) and E (290 °C) stream temperatures at the most bottom P11. The lower temperatures at P10 are the result of additional heat losses through the non-insulated walls and some mixing with the cold K stream. As expected, temperature differences between P10 and P11 are the most pronounced in the radial centre, despite using the hot D stream to counteract the suction effect. The P11(l) and P11(r) data confirm good symmetry at the hot air inlet. The P10 (l) and P10(r) temperature profiles show, however, up to 10 °C difference at given distance from the cylindrical wall. Hot air expansion or the counter-current operation can be at the origin of some symmetry breaking.

4. Water evaporation test

A video showing the water atomized from the top against the hot air coming from the bottom hot air distribution chamber can be seen in Supplementary material.

The flow pattern is somewhat dynamic, with the spray partially deflected and rotating in the chamber. This may indicate a partial bypass of hot air and droplets. Fig. 5 shows time averaged temperature profiles measured during water evaporation at 9.8 g/s, with other operating conditions as in the dry run. Whereas a temperature drop indicates evaporation at a given location, wetting of the thermocouple can eventually affect the actual temperature reading.

Looking at the cyclonic extension (Fig. 5a), good radial symmetry is observed. Comparing temperatures from the dry run (Fig. 4a) and during water evaporation (Fig. 5a) shows that in the vicinity of the cylindrical wall, the temperatures at P1 and P2 elevation have only slightly decreased and remain determined by the H stream. At P3 and P4 elevation, however, the near-wall temperatures have dropped by ca. 45 °C. More radially inward, all air temperatures have dropped by ca. 50 °C, but there is no indication of liquid water reaching the cyclonic extension.

Inside the spray drying chamber, the temperatures are strongly affected by the water evaporation, as seen comparing Figs. 5b–f and Figs. 4b–f. Water evaporation significantly decreased the temperature in the radial centre of the chamber. Temperatures below 100 °C indicate potential presence of liquid water. Such temperatures are observed as low as P9, ca. 9 cm above the bottom vortex chamber. At P5-P8 elevation, radial symmetry is relatively well conserved, with only a slight deviation of the water spray towards the 0° and 90° orientations. At P9 elevation, the asymmetry is more pronounced, with lower temperatures at the 0° and 90°, compared to the 180° and 270° orientations. The temperatures in the periphery have increased from ca. 100 °C to 120–140 °C. The water spray penetrating the counter current introduced hot air pushes the latter radially outward, leading to increased mixing with the mild temperature air introduced in the periphery. A clearly distinct radially central zone and periphery are, however, maintained, essential for the RMD working principle. Furthermore, radial expansion of the hot air increases the contact time between the latter and the droplets / particles, and as such the RMD efficiency.

The temperature profiles in the hot air distribution chamber (Fig. 5g) show that some water vapor and cooled air reaches the P10 elevation in the radial centre, but with temperatures just reaching 100 °C at some locations, the presence of liquid water is not expected. Near the cylindrical wall, hardly any penetration of water vapor and cooled air is observed. Comparison of the P10(l) and P10 (r) profiles shows radial asymmetry, however, which can be problematic for fouling. At the lowest position P11, the effect of evaporating water in the RMD is minimal. A slight asymmetry comparable to that detected in the dry run (Fig. 4g) is also observed.

A repetitive water evaporation test was carried out. Fig. 6 shows the measured temperature profiles through port P9. Overall, the observed profiles are similar. Some differences can be attributed to deviations from symmetry, although in both tests the atomized water preferentially penetrates at the 0° and 90° orientations.

5. Spray drying test

Figs. 7a and b show the evolution in time of the amount of water / maltodextrin solution consumed and of the air exit temper-

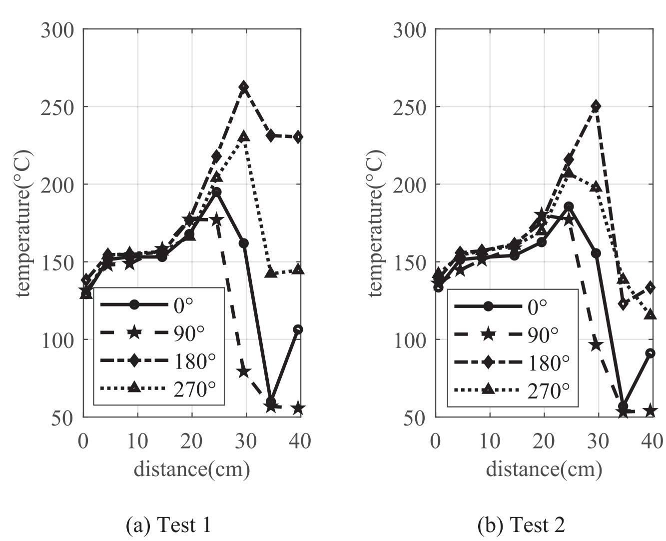

Fig. 6. Repetitive water evaporation test showing measured temperature profiles at P9.

ature during the different phases of the spray drying test. Following starting evaporation of water at 10.4 g/s, it takes ca. 35 min for the steady state air exit temperature of 209 ± 1 °C to decrease to its new steady state value of 164 ± 1 °C. When switching from water to the maltodextrin solution, the air exit temperature decreased within 25 s by 9 °C, but then increased again to 166 °C, that is 2 °C higher than during the water evaporation (Fig. 7b). With the applied shut-down procedure, the increase in air exit temperature could be limited to 8 °C, maximum reached 14 s after stopping the liquid feed, after which the air exit temperature steadily decreased.

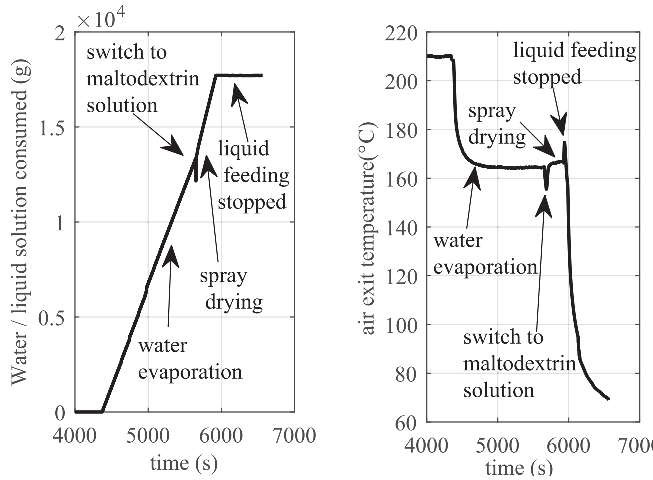

(a) Mass of water / maltodextrin solution consumed (g) versus time (s)

(b) Air exit temperature (°C)

Fig. 7. (a) Amount of water / maltodextrin solution consumed (g) and (b) air exit temperature versus time (s) during the different phases of the spray drying test, as indicated in the figures.

Fig. 8 shows pictures of different elements of the RMD unit after the spray drying test. Powder is recovered from the collection bins, from inside the spray drying chamber and from the cyclone installed in the main air exhaust line. Very fine powder is not captured by the cyclone and reaches the filter and exhaust. Within the spray drying chamber, powder deposits are more symmetrical in the top than in the bottom portion. The observed asymmetry is related to the deposits found in the hot air inlet which partially block the entering hot air and accelerate further fouling. Some deposits occurred around the sleeve protecting the spray nozzles and in the hot air distribution chamber. The latter are brown due to prolonged high temperature exposure. No fouling of the air splitter integrated deeper inside the hot air distribution chamber occurred. Deposits on the nozzle tips were not observed, which is essential for keeping them functional and demonstrates proper functioning of the protective sleeve with the dedicated air streams. The deposits in the hot air distribution chamber indicate slower evaporation from the solution as compared to water due to crust formation introducing diffusion limitations. As a result, the drying particles stay heavier and are deflected less rapidly by the counter current hot air stream. Table 3 shows the amount of powder recovered at the different locations. About 9 % of the injected solution ends up fouling the hot air inlet, implying that ca. 90 % of the droplets / powder is properly deflected by the incoming hot air. Ca.

(a) Bottom part of the spray drying chamber with the central hot air inlet

(b) Top part of the spray drying chamber with centrally the passage to the cyclonic extension and all the way at the top the main air outlet

(c) The hot air distribution chamber

(d) Non-powderous deposition

(e) Powder deposition in the spray drying chamber

Fig. 8. Pictures of various parts of the RMD unit after the spray drying test. Most of the powder was collected in the bins connected to the bottom and top collection ports.

Table 3
Amount of maltodextrin powder recovered at different locations in the RMD unit following spray drying (g).

Bottom Collection Port 1	204.7
Bottom Collection Port 2	155.4
Top Collection Port	263.0
Spray drying chamber	220.4
Hot air distribution chamber	152.8
Cyclone	271.2
Other (filter, loss of fines)	468.5

36 % of the injected maltodextrin left as powder via the collection ports. A significant fraction of the maltodextrin is retrieved as powder inside the spray drying chamber, however. As during spray drying, powder is seen rotating in the chamber periphery, the observed accumulation can be attributed to inefficient evacuation via the collection ports or some stickiness of the powder to the walls. The powder collected from the walls brushes, however, easily off and its properties were also determined. Verification by means of a thermal imaging camera showed the outer wall temperature of the spray drying chamber did not exceed 100 °C, explaining limited stickiness of the maltodextrin particles to the wall. No deposits of maltodextrin were found in the cyclonic extension, indicating drying is completed in the spray drying chamber, as was also observed during the water evaporation test. Ca. 16 % of the maltodextrin is recovered as fine powder in the downstream cyclone and 27 % ends up in the filters and exhaust. It should be noted that the cyclone was not specifically designed for the droplet size distribution produced by the selected nozzles.

6. Powder characterization

The powder collected from the different locations is characterized by means of optical microscopy, Scanning Electron Microscopy (SEM), and particle size distribution and roundness measurements. Fig. 9 shows the optical microscopy pictures with a 100 µm reference bar. The particles are hollow and relatively spherical, with little to no agglomeration. Whereas the particles collected from the various collection ports and from inside the spray drying chamber are quite similar, the particles retrieved in the cyclone are clearly finer. Hollow particles are explained by rapid initial drying and crust formation. When a crust forms, particles can explode if trapped water evaporates and cannot be sufficiently fast evacuated. This is, however, not observed, indicating efficient evacuation of the initially dried particles from the radial centre to the periphery where slower final drying takes place in contact with mild temperature air.

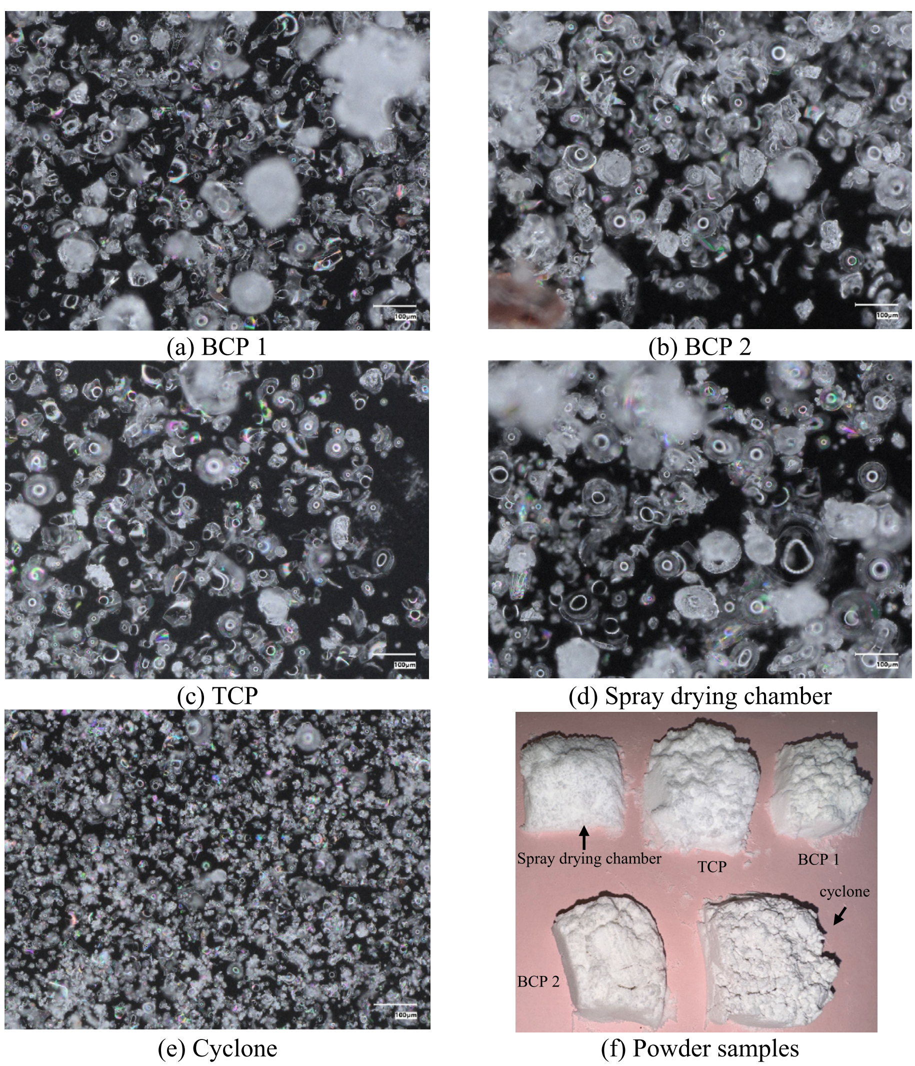

Fig. 9. (a)-(e) Optical microscopy pictures and (f) samples of the powder collected at the bottom (BCP1 and BCP2) and top (TCP) collection ports, inside the spray drying chamber, and in the cyclone.

Fig. 10 shows SEM pictures of the different collected powders. The image resolution and other information are provided in the image itself. Samples were deposited on a carbon tape and non-sticky dust removed blowing a laminar flow of compressed air. The obtained stub was then covered with a thin Au/Pd-layer using a Balzer plasma sputtering machine operated for 60 s with a 30 mA current. As such, the particles are covered with a conductive layer to prevent charging in the scanning electron microscope (SEM). The Zeiss Ultra 55 microscope used for the imaging did not possess low vacuum capabilities, and only high vacuum conditions (< 1e-5 mbar) could be imposed. As a result, the produced hollow particles exploded and fragmented particle remains are observed in the SEM pictures. The fragmentation under the SEM vacuum confirms that hollow particles were produced in the RMD. The images also show very little porosity, at least at the observed scale. Approximate shell thicknesses can be derived that are respectively in the range 3–9 μ m for the powder collected from BCP1, 3–23 μ m for that from BCP2, 2–4 μ m for that from the TCP, 4–11 μ m for that from the main RMD chamber, and 2–4 μ m for that from the cyclone.

Fig. 11a shows the Particle Size Distributions (PSD) of the powder collected at the different locations, measured using a Microtrac Turbo Sync particle characterising machine [31]. A wet dispersion system was used to separate the particles and produce a uniform distribution. Isopropanol with a refractive index of 1.38 was used as solvent. Once wetted, the fully dispersed particles enter a flow loop. Laser beam diffraction on the dispersed particles is measured by a detector array. Additionally, pictures are taken by a high-speed camera while a LED light source illuminates the sample. Dynamic image processing software then derives the particle size distribution. The observed particle size distributions are directly related to that of the injected droplets, significant agglomeration not taking place. The PSD measurements confirm that similar powder is collected from both bottom collection ports with an average particle size of 34 μm and 36 μm respectively. The mean particle size of the powder (Table 4) from the top collection port is slightly smaller at 28 μm, whereas that of the powder retrieved from the spray drying chamber is somewhat larger at 42 μm. The average size of the powder recovered from the collection ports and inside the spray drying chamber is within the range of commercial interest. With an average particle size of ca. 19 μm, the powder captured by the cyclone is significantly smaller. Under the action of the centrifugal force in the RMD, larger particles are well retained, whereas there is a significant loss of the smallest particles with the air exiting the RMD. The intensified segregation of particles of dif-

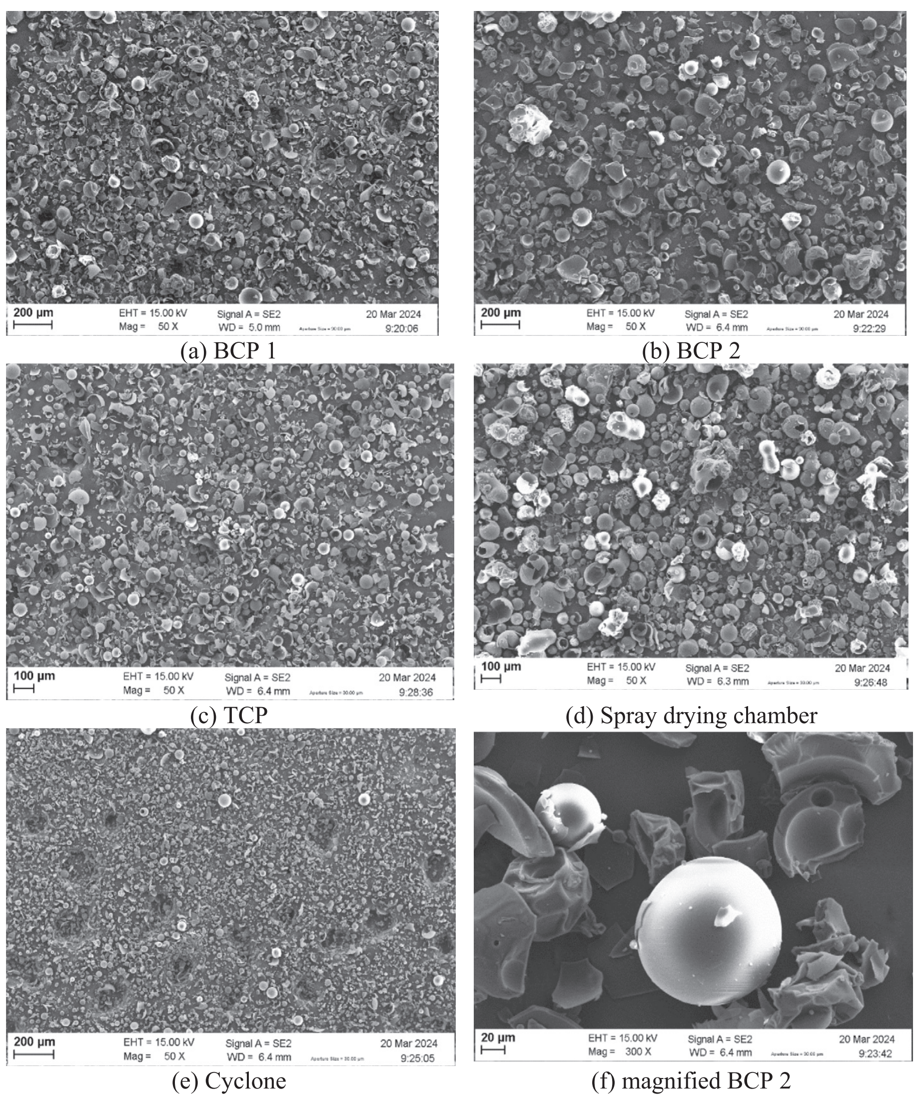

Fig. 10. (a)-(e) SEM pictures of the powder collected at the bottom (BCP1 and BCP2) and top (TCP) collection ports, inside the spray drying chamber, and in the cyclone (f) magnified view of powder from BCP2.

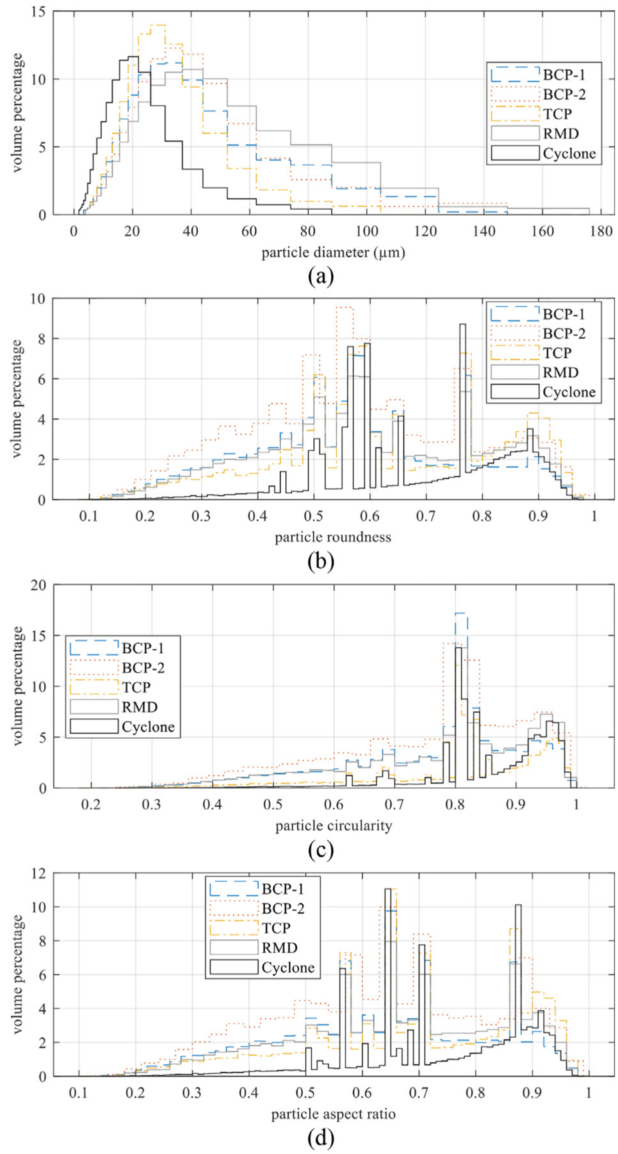

Fig. 11. Characterization of the powder collected at the bottom (BCP1 and BCP2) and top (TCP) collection ports, inside the spray drying chamber (RMD), and in the cyclone: (a) Particle Size Distribution; (b) Particle roundness distribution; (c) Particle circularity distribution; (d) Particle aspect ratio distribution.

Table 4
Average particle diameter of the powder from various collection points.

Collection point	BCP 1	BCP 2	TCP	Spray drying chamber/RMD	Cyclone
<Diameter> (μm)	34.4	36.0	28.5	41.5	19.1

ferent size and/or density under the action of the centrifugal force can be of practical interest and was earlier observed and experimentally and numerically studied in vortex chamber-generated rotating fluidized beds [32 24].

Fig. 11b shows the roundness distribution curves of powder samples from the various collection points, generated by MATLAB software's histogram function [33]. Microtrac provides information on the roundness, circularity and aspect ratio of a powder sample. A total of 38629, 8388, 43839, 36,334 and 76,748 particles were analysed for the samples taken from BCP1, BCP2, the TCP, the RMD main chamber and the cyclone, respectively. The average roundness and the percentage of particles with roundness above 0.8 are reported in Table 5. The particle roundness distribution curves are similar and somewhat bimodal, except for the powder from the cyclone which has a maximum around 0.9. The average roundness for the BCP1, BCP2, TCP, RMD and cyclone samples are 0.573, 0.574, 0.630, 0.601 and 0.685, respectively and 10.5 %, 13.2 %, 23.7 %, 18.5 % and 30.1 % of the powder having a roundness above 0.8. Apart from roundness, other important shape factors are circularity (Fig. 11c) and aspect ratio (Fig. 11d). Table 6 shows the average circularity and the percentage of particles with above 80 % circularity. Most of the powder has a circularity above 0.7, with for respectively BCP1, BCP2, the TCP, the RMD main chamber, and the cyclone, an average circularity of 0.76, 0.76, 0.80, 0.77 and 0.85, and 54.3 %, 44.3 %, 67.7 %, 56.7 % and 82.1 % of the powder having a circularity above 0.8. The circularity is seen to be significantly higher than the roundness, which indicates rough surfaces over the edges. Table 7 shows the average aspect ratio and the percentage of particles with above 80 % aspect ratio. The latter is defined as FWidth/FLength (2D), where FLength = Maximal distance between parallel tangents, FWidth = Minimal distance between parallel tangents. Most of the powder has an aspect ratio above 0.6, with the powder from the BCP1, BCP2, TCP, RMD main chamber and cyclone having an average aspect ratios of 0.63, 0.63, 0.68, 0.66 and 0.73, respectively, and 21.2 %, 21.2 %, 33.5 %, 27.4 % and 43.4 % of the powder having an aspect ratio above 0.8. Combining the observations of particle size and shape distribution, the finer powder has a superior roundness, which can be expected in spray drying.

Table 8 compares Laser diffraction data of the particle mean volume diameter with the particle size distribution found from sieving the particles using four sieves with mesh width 50 μm, 100 μm, 150 μm and 450 μm. The particles were sieved using a Retsch vs 1000 sieving apparatus [34] which was operated at amplitude 60 for 120 min using the particles as collected without adding chemicals. It is seen that only for the powder collected from the cyclone, the data obtained from Laser diffraction and from sieving correspond relatively well. For the samples collected through the other ports and from inside the RMD, significant fractions of larger-diameter particles are found when using the sieving technique. This indicates a certain degree of agglomeration of produced fine powder by electrostatic or cohesive forces – these agglomerates being broken down when using the Laser diffraction technique.

The moisture content of the produced powder was determined keeping samples in an oven at 70 °C for 2 h and measuring the weight change. A moisture content of respectively 0.8 %, 0.9 %, 0.7 %, 0.8 % and 0.7 % was found in the samples collected from the BCP1, BCP2, TCP, RMD main chamber and cyclone.

7. Energy efficiency

a) Measured energy efficiency.

The energy efficiency was determined from a water evaporation test evaporating 15.6 g/s of water. From the required heat of evaporation and from the power consumption by the five heaters that are used, an energy efficiency of 53.8 % is obtained for this non-

Table 5
Average roundness of the powder from various collection points.

Collection point	BCP 1	BCP 2	TCP	Spray drying chamber/RMD	Cyclone
Average roundness	0.573	0.574	0.630	0.601	0.685
More than 80 % roundness	10.4 %	13.2 %	23.7 %	18.5 %	30.1 %

Table 6
Average circularity of the powder from various collection ports.

Collection point	BCP 1	BCP 2	TCP	Spray drying chamber/RMD	Cyclone
Average circularity	0.76	0.76	0.80	0.77	0.85
More than 80 % circularity	54.3 %	44.3 %	67.7 %	56.7 %	82.1 %

Table 7
Average aspect ratio of the powder from various collection ports.

Collection point	BCP 1	BCP 2	TCP	Spray drying chamber/RMD	Cyclone
Average aspect ratio	0.63	0.63	0.68	0.66	0.73
More than 80 % aspect ratio	21.2 %	21.2 %	33.5 %	27.4 %	43.4 %

Table 8
Sieve analysis of the powder from various collection points and comparison with Laser diffraction data.

	Laser diffraction – % particles with mean volume diameter 0–52 μm	Sieve analysis – m% 0–50 μm	Sieve analysis – m% 50–100 μm	Sieve analysis – m% 100–150 μm	Sieve analysis – m% 150–450 μm	Sieve analysis – m% >450 μm
BCP1	76.01	42.55	40.52	11.10	4.95	0.85
BCP2	73.43	34.21	51.71	9.63	3.56	0.86
TCP	87.17	64.13	31.2	3.67	0.65	0.32
Spray drying chamber/RMD	76.44	4.19	24.53	17.85	39.20	14.21
Cyclone	95.71	89.8	7.8	2.1	0.10	0.10

optimized pilot scale RMD, where conventional spray dryers offer 40–60 % energy efficiency. The actual energy efficiency should account for the energy consumption by the two compressors (68.9 kW and 18.5 kW), the blower (9.74 kW) and the pump (1/2 HP) that are used to feed the drying air and liquid feed. The actual energy consumption by these devices during the tests is, however, not measured. In a commercial RMD unit, the energy efficiency can be optimized by using a highly efficient air blower and by reducing various heat losses. Heat recovery from the air exiting can be considered. The exiting air can eventually also be partially recycled and used for the hot air feed streams after reheating, if it is powder free.

b) Theoretical energy efficiency and evaporation capacity.

Efficient contact between a dense droplet cloud and the hot air that is fed is essential for achieving a high energy efficiency and evaporation capacity. The pilot plant RMD was designed for feeding ca. 1,500 kg/h hot air in the radially central zone (streams B, D and E) at about 350 °C, and ca. 700 kg/h mild temperature or cold air along the periphery and through the sleeve outer surface. The latter is split in a warm stream F at ca. 130 °C with a design mass flow rate of around 200 kg/h for maintaining a dense rotating fluidized bed of powder undergoing final drying, and cold streams C, G, H and K at room temperature or as heated by the compressor.

Taking the experimental example water evaporation test case and accounting for the heat capacity of air of 1.005 kJ/kg/°C and heat of evaporation of water of 2256.5 kJ/kg, the theoretical water evaporation capacity of the heat provided by the different air streams can be estimated as:

- Hot air streams B, D and E: 1308 kg air/h at 350 °C (air heated from 20 °C to 350 °C): assuming 50 % of the provided heat is effectively used, this allows to evaporate 1308 kg air/h * 330 °C * 1.005 kJ/kg air/°C * 0.5 / 2256.5 kJ/kg water = 96.12 kg water/h.
- Warm air stream F: 192 kg air/h at 130 °C (air heated from 20 °C to 130 °C): assuming an 80 °C temperature drop by the final drying in the periphery, this allows to evaporate 192 kg air/h * 80 °C * 1.005 kJ/kg air/°C / 2256.5 kJ/kg water = 6.84 kg water/h.

The cold streams C, G, J and H (at least 475 kg air/h at room temperature) are assumed not to contribute to the water evaporation but are needed for maintaining a relatively dry (< 45 g water/kg air) and cold (< 100 °C) air layer along the periphery and the sleeve in order to prevent powder stickiness and for generating a sufficiently high centrifugal force in order to accumulate the produced powder along the periphery.

Using the above numbers, the total heat consumed to heat the various air streams amounts to 1308 kg air/h * 330 °C * 1.005 kJ/kg air/°C + 192 kg air/h * 110 °C * 1.005 kJ/kg air/°C = 455 MJ/h. The total amount of heat used for the evaporation of water amounts to 102.96 kg water/h * 2256.5 kJ/kg water = 232.33 MJ/h, bringing the energy efficiency to 232.33/455 = ~ 51 %. The theoretical analysis of the energy efficiency and evaporation capacity is summarized in Table 9. In a commercial scale unit, the fraction of heat from the hot air streams that is effectively used for evaporation can be higher than the 50 % assumed in this calculation, bringing the overall efficiency to > 65 %. As such, a 1975 kg/h total air stream in the 0.45 m^3 pilot plant is expected to be able to vaporize 103 kg/h of water contained in a 172 kg/h maltodextrin solution at 40 % concentration, in order to produce 69 kg/h dry powder.

8. Conclusions

The paper presents a first maltodextrin spray drying study with a pilot scale Radial Multizone Dryer (RMD). The RMD combines fast initial drying in the radial centre of the spray drying chamber with slower final drying in the periphery. In the radial centre, hot air and atomized liquid are injected axially and counter-current. Rapid evacuation of the initially dried particles to the periphery is achieved by introducing a rotational motion in the chamber by means of two vortex chambers. The mild temperature air injected in those vortex chambers ensures proper conditions for final drying in the periphery. Generating a centrifugal pressure difference between the two vortex chambers allows controlling the axial motion in the periphery. A cyclonic extension on top of the spray drying chamber aims at optimizing gas-solids separation.

Detailed temperature measurements during dry run and water evaporation tests allowed gaining insight in the functioning of the

Table 9
Theoretical energy efficiency and evaporation capacity analysis.

Air stream	Air mass flow rate (kg/h)	Air feed temp. (°C)	Heat supply (MJ/h)	Expected temp. drop (°C)	Energy efficiency (%)	Water evaporation capacity (kg/h)	Heat of evaporation (MJ/h)
B	70	350 °C	433.8	165 °C	50 %	96.12	216.9
D	472						
E	766						
F	192	130 °C	21.2	80 °C	73 %	6.84	15.4
G + H + C + J	475 min.	Room temp.	N.A. – for preventing powder stickiness and generating centrifugal force				
Total	1975	N.A.	455	154 °C	51 %	102.96	232.3

RMD and selecting proper conditions for a spray drying test. The measurements confirmed the working principle of the RMD and confirmed limited mixing between the air injected in the radial centre and in the periphery, fast initial drying and a sufficiently low temperature in the periphery. Efficient and complete evaporation could be achieved at 15.6 g H_2O/s. The measured energy efficiency is close to the expected value of 51 %.

A spray drying test under identical operating conditions as during water evaporation but maintaining the water evaporation duty produced fine maltodextrin powder. The latter left the RMD through the foreseen collection ports, remained in the spray drying chamber or, a finer fraction, was lost through the main air exit and captured by a downstream cyclone. Minor deposits of solid material were found at the exit of the hot air distribution chamber. This indicates somewhat slower water evaporation from the maltodextrin solution compared to pure water droplets, as can be expected. Nevertheless, such deposits have to be avoided, as they get burned rapidly and cause asymmetric distribution of hot air in the spray drying chamber. About 90 % of the atomized solution is properly deflected, with about 36 % of the maltodextrin recovered via the collection ports, and 9 % was fouling the hot air inlet. A significant amount of powder was recovered from the spray drying chamber itself, none was found in the cyclonic extension. Finally, about 16 % of the maltodextrin is found in the downstream cyclone as fine powder and 27 % finds its way to the filter and exhaust. The results show that a more efficient evacuation of the produced powder and optimization of the operating conditions is needed to avoid excessive accumulation of powder in the spray drying chamber and initial stickiness to the cylindrical wall. With respect to the latter, optimization of the start-up procedure is also to be considered. Cyclone redesign and a controlled wall temperature may also further improve the powder recovery efficiency and energy efficiency. Analysis of the produced powder collected at the different locations by means of optical microscopy, SEM and particle size and roundness distribution measurements indicates that very little to no agglomeration of the produced powder occurred. The optical microscopy pictures further reveal that hollow and relatively spherical particles were produced. The particle size distribution is directly related to the droplet size distribution that was generated by the spray nozzles. The particle size distribution of the powders from the various collection ports and from inside the spray drying chamber are not very different, with an average particle size of ca. 30–40 μm – on the lower end of the commercially interesting size. The powder retrieved from the downstream cyclone was significantly smaller with an average size of 19 μm. The action of the centrifugal force in the RMD as such provides some segregation of the produced powder, which can be of practical interest. Laser diffraction measurements of the particle roundness, circularity and aspect ratio confirmed the visual observation that relatively spherical particles were produced. The average particle roundness, circularity and, respectively, aspect ratio are 0.5735 / 0.76 / 0.63 for the powder that left through the bottom collection ports, 0.601 / 0.77 / 0.66 for the powder retrieved in the spray drying chamber, 0.630 / 0.80 / 0.68 for the powder that left through the top collection port and 0.685 / 0.85 / 0.73 for the fines in the downstream cyclone. The moisture content of the produced powder was in the range 0.7–0.9 %. The observed shape is, hence, more spherical as the particles are smaller. Comparison with a conventional particle sieving analysis shows some agglomeration due to electrostatic or cohesive forces. The analysis furthermore indicates some irregularities over the edges of larger particles. Finally, SEM pictures show that the produced particles are hollow and with a low porosity shell.

CRediT authorship contribution statement

Santanu Dey: Writing – original draft, Data curation. **Thomas Tourneur:** Data curation. **Axel de Broqueville:** Supervision, Methodology, Investigation, Formal analysis, Conceptualization. **Armand Béché:** Investigation, Data curation. **Juray De Wilde:** Writing – review & editing, Writing – original draft, Supervision, Resources, Project administration, Methodology, Investigation, Funding acquisition, Formal analysis, Data curation, Conceptualization.

Declaration of competing interest

The authors declare that they have no known competing financial interests or personal relationships that could have appeared to influence the work reported in this paper.

Acknowledgements

Authors would like to acknowledge the support from the staff of CREDEM and LACAMI platform of UCLouvain, especially Hervé Delafontaine, Luc Wautier and Marc Sinnaeve for their maintenance support, help with assembling the RMD unit and resolving technical issues. Victor Lhoest, and Frank Hesbois are acknowledged for support related to electronics and Arnaud Lion for the technical drawings of the set-up. The authors thank Frédéric Van Wonterghem for his help with the particle size distribution measurements. The authors thank Olivier Poncelet for his help with the sieve analysis.

This project was managed by the Dutch Institute for Sustainable Process Technology (ISPT) and financed through the Rijksdienst voor Ondernemend Nederland (RVO) and Avebe, Corbion and Givaudan. Special thanks to Anne van der Zwaan and Rick Kirpenstein for managing the project. Thank you, Professor AK Pozarlik, for your valuable collaboration within the Engender project.

Appendix A. Supplementary data

Supplementary data to this article can be found online at https://doi.org/10.1016/j.apt.2025.105148.

References

[1] G.F. Froment, K.B. Bischoff, J. De Wilde, Chemical Reactor Analysis and Design , 3rd ed., John Wiley & Sons, Inc. , 2011.

[2] J. De Wilde, Gas–solid fluidized beds in vortex chambers, Chem. Eng. Process. 85 (2014) 256–290. https://doi.org/10.1016/j.cep.2014.08.013.

[3] M. Friedle, G.B. Marin, G.J. Heynderickx, Operational range of a gas-solid vortex unit, Powder Technol. 338 (2018) 702–715. https://doi.org/10.1016/j.powtec.2018.07.062.

[4] J.Z. Kovacevic, M.N. Pantzali, G.J. Heynderickx, G.B. Marin, Bed stability and maximum solids capacity in a gas–solid vortex reactor: experimental study, Chem. Eng. Sci. 106 (2014) 293–303. https://doi.org/10.1016/j.ces.2013.11.018.

[5] L.M. Kochetov, B.S. Sazhin, E.A. Karlik, Hydrodynamics and heat exchange in vortex drying chambers, Chem. Pet. Eng. 5 (1969) 688–690. https://doi.org/10.1007/BF01136999.

[6] M.A. Howley, R. Pfeffer, The hydrodynamics of a rotating fluidized bed, in: Proceedings of AIChE Annual Meeting, Cincinnati, OH, 2005., Ohio, 2005.

[7] S. Dutta, C. Loha, P.K. Chatterjee, A. Kumar Sadhukhan, P. Gupta, Numerical investigation of gas-particle hydrodynamics in a vortex chamber fluidized bed, Adv. Powder Technol. 29 (2018) 3357–3367. https://doi.org/10.1016/j.apt.2018.09.014.

[8] U. Jamil Ur Rahman, A. Krzysztof Pozarlik, T. Tourneur, A. de Broqueville, J. De Wilde, G. Brem, Numerical Study toward Optimization of Spray Drying in a Novel Radial Multizone Dryer, Energies (Basel) 14 (2021) 1233. https://doi.org/10.3390/en14051233.

[9] X. Lang, Y. Ouyang, S. Dutta, S. Chen, L. Li, G. Heynderickx, K.M. Van Geem, Hydrodynamic study of the operating window of a stator-rotor vortex chamber reactor, Powder Technol. 427 (2023) 118749. https://doi.org/10.1016/j.powtec.2023.118749.

[10] U. Jamil Ur Rahman, A.K. Pozarlik, G. Brem, Experimental analysis of spray drying in a process intensified counter flow dryer, Drying Technol. 40 (2022) 3128–3148. https://doi.org/10.1080/07373937.2021.2004160.

[11] J. De Wilde, A. de Broqueville, Rotating fluidized beds in a static geometry: Experimental proof of concept, AIChE J 53 (2007) 793–810. https://doi.org/10.1002/aic.11139.

[12] J. De Wilde, A. de Broqueville, Experimental investigation of a rotating fluidized bed in a static geometry, Powder Technol. 183 (2008) 426–435. https://doi.org/10.1016/j.powtec.2008.01.024.

[13] P. Eliaers, J. De Wilde, Drying of biomass particles: experimental study and comparison of the performance of a conventional fluidized bed and a rotating fluidized bed in a static geometry, Drying Technol. 31 (2013) 236–245. https://doi.org/10.1080/07373937.2012.726304.

[14] A. Mania, Christophe Guy, Jamal Chaouki, BIOMASS GASIFICATION IN ROTATING FLUIDIZED BED, in: The 13th International Conference on Fluidization - New Paradigm in Fluidization Engineering, 2010.

[15] A. de Broqueville, J. De Wilde, Numerical investigation of gas-solid heat transfer in rotating fluidized beds in a static geometry, Chem. Eng. Sci. 64 (2009) 1232–1248. https://doi.org/10.1016/j.ces.2008.11.009.

[16] A. Dutta, R.P. Ekatpure, G.J. Heynderickx, A. de Broqueville, G.B. Marin, Rotating fluidized bed with a static geometry: guidelines for design and operating conditions, Chem. Eng. Sci. 65 (2010) 1678–1693. https://doi.org/10.1016/j.ces.2009.11.013.

[17] W. Zhang, A review of techniques for the process intensification of fluidized bed reactors, Chin. J. Chem. Eng. 17 (2009) 688–702. https://doi.org/10.1016/S1004-9541(08)60264-5.

[18] S. Dutta, C. Loha, P.K. Chatterjee, A.K. Sadhukhan, P. Gupta, Study the particle loss from vortex chamber fluidized bed with different conditions, Adv. Powder Technol. 32 (2021) 3499–3505. https://doi.org/10.1016/j.apt.2021.08.004.

[19] Combustion in Vortex Chambers with a Fluidized Particle Bed, Физика Горения и Взрыва 51 (2015). https://doi.org/10.15372/FGV20150602.

[20] R.W. Ashcraft, G.J. Heynderickx, G.B. Marin, Modeling fast biomass pyrolysis in a gas–solid vortex reactor, Chem. Eng. J. 207–208 (2012) 195–208. https://doi.org/10.1016/j.cej.2012.06.048.

[21] S. Dutta, S. Roy, X. Lang, S. Chen, R. Kumar, C. Loha, T. Verspeelt, K.M. Van Geem, G.J. Heynderickx, Y. Ouyang, Process intensification of CO_2 desorption in a gas–liquid vortex reactor, Ind. Eng. Chem. Res. 63 (2024) 10544–10553. https://doi.org/10.1021/acs.iecr.4c00904.

[22] S. Chen, X. Lang, A. Kourou, S. Dutta, K.M. Van Geem, Y. Ouyang, G.J. Heynderickx, Enhancing CO_2 capture efficiency: computational fluid dynamics investigation of gas-liquid vortex reactor configurations for process intensification, Chem. Eng. J. 493 (2024) 152535. https://doi.org/10.1016/j.cej.2024.152535.

[23] A. Gonzalez-Quiroga, P.A. Reyniers, S.R. Kulkarni, M.M. Torregrosa, P. Perreault, G.J. Heynderickx, K.M. Van Geem, G.B. Marin, Design and cold flow testing of a gas-solid vortex reactor demonstration unit for biomass fast pyrolysis, Chem. Eng. J. 329 (2017) 198–210. https://doi.org/10.1016/j.cej.2017.06.003.

[24] J. De Wilde, G. Richards, S. Benyahia, Qualitative numerical study of simultaneous high-G-intensified gas–solids contact, separation and segregation in a bi-disperse rotating fluidized bed in a vortex chamber, Adv. Powder Technol. 27 (2016) 1453–1463. https://doi.org/10.1016/j.apt.2016.05.005.

[25] V. Verma, T. Li, J. De Wilde, Coarse-grained discrete particle simulations of particle segregation in rotating fluidized beds in vortex chambers, Powder Technol. 318 (2017) 282–292. https://doi.org/10.1016/j.powtec.2017.05.037.

[26] P. Eliaers, A. de Broqueville, A. Poortinga, T. van Hengstum, J. De Wilde, High-G, low-temperature coating of cohesive particles in a vortex chamber, Powder Technol. 258 (2014) 242–251. https://doi.org/10.1016/j.powtec.2014.03.033.

[27] T. Li, S. Pannala, C. Dittrich, D. West, A numerical scale-up study of annular fluidized bed reactor with high centrifugal acceleration, Powder Technol. 442 (2024) 119893. https://doi.org/10.1016/j.powtec.2024.119893.

[28] J. De Wilde, S. Dutta, J.R. Pati, A. de Broqueville, Experimental study of the temperature distribution and water evaporation in an axial dual-zone vortex chamber spray dryer, Drying Technol. 40 (2022) 2794–2811. https://doi.org/10.1080/07373937.2021.1966635.

[29] A. De Broqueville, J. De Wilde, T. Tourneur, Device for treating particles in a rotating fluidized bed, US Patent 11154831B2, 2021.

[30] P.D. Hede, P. Bach, A.D. Jensen, Two-fluid spray atomisation and pneumatic nozzles for fluid bed coating/agglomeration purposes: a review, Chem. Eng. Sci. 63 (2008) 3821–3842. https://doi.org/10.1016/j.ces.2008.04.014.

[31] Microtrac Turbo Sync particle characterising machine, https://www.microtrac.fr/fr/produits/analyse-taille-forme-particules/diffraction-laser/sync/, (n.d.).

[32] J.M. Weber, R.C. Stehle, R.W. Breault, J. De Wilde, Experimental study of the application of rotating fluidized beds to particle separation, Powder Technol. 316 (2017) 123–130. https://doi.org/10.1016/j.powtec.2016.12.076.

[33] Mathworks, MATLAB histogram Histogram plot, (n.d.). https://nl.mathworks.com/help/matlab/ref/matlab.graphics.chart.primitive.histogram.html (accessed June 21, 2025).

[34] Retsch Sieve Analysis , (n.d.). https://www.retsch.com/files/8785/expert-guide-sieving.pdf (accessed June 21, 2025).